Chinese Chemical Letters 35 (2024) 109377

Contents lists available at ScienceDirect

Chinese Chemical Letters

journal homepage: www.elsevier.com/locate/cclet

Regulating the key performance parameters for Hg-based IR NLO chalcogenides *via* bandgap engineering strategy

A-Yang Wang[a,b,c,1], Sheng-Hua Zhou[a,b,d,1], Mao-Yin Ran[a,b,d], Xin-Tao Wu[a,b], Hua Lin[a,b,*], Qi-Long Zhu[a,b,*]

[a] State Key Laboratory of Structural Chemistry, Fujian Institute of Research on the Structure of Matter, Chinese Academy of Sciences (CAS), Fuzhou 350002, China
[b] Fujian Science & Technology Innovation Laboratory for Optoelectronic Information of China, Fuzhou 350108, China
[c] College of Chemistry, Fuzhou University, Fuzhou 350108, China
[d] University of Chinese Academy of Sciences, Beijing 100049, China

ARTICLE INFO

Article history:
Received 9 November 2023
Revised 4 December 2023
Accepted 6 December 2023
Available online 12 December 2023

Keywords:
Hg-based chalcogenides
IR nonlinear material
Structure-activity relationship
Wide energy gap
Bandgap engineering strategy

ABSTRACT

Recently, non-centrosymmetric (NCS) Hg-based chalcogenides have garnered significant interest due to their strong second-harmonic-generation intensities (d_{eff}), making them attractive candidates for infrared nonlinear optical (IR-NLO) application. However, achieving both wide band gaps (E_g) and large phase-matched d_{eff} simultaneously in these materials remains a challenge due to their inherent constraints on each other. In this research, we have successfully obtained two quaternary NCS Hg-based chalcogenides, $Rb_2HgGe_3S_8$ and $Cs_2HgGe_3S_8$, by implementing a bandgap engineering strategy that involves alkali metal introduction and Hg/Ge ratio regulation. Both compounds consist of 2D $[HgGe_3S_8]^{2-}$ anionic layers made of 1D $[HgGeS_6]^{6-}$ chains and dimeric $[Ge_2S_6]^{4-}$ polyhedra arranged alternately, and the charge-balanced Rb^+/Cs^+ cations located between these layers. Remarkably, $Rb_2HgGe_3S_8$ and $Cs_2HgGe_3S_8$ exhibit overall properties required for promising IR-NLO materials, including sufficient PM d_{eff} (0.55–0.70 × $AgGaS_2$@2050 nm), large E_g (3.27–3.41 eV), giant laser-induced damage thresholds (17.4–19.7 × $AgGaS_2$@1064 nm), broad optical transmission intervals (0.32–17.5 μm), and suitable theoretical birefringence (0.069–0.086@2050 nm). Furthermore, in-depth theoretical analysis reveals that the exceptional IR-NLO performance is attributed to the synergy effects of distorted $[HgS_4]$ and $[GeS_4]$ tetrahedra. Our study provides a useful strategy for enhancing the E_g and advancing Hg-based IR-NLO materials, which is expected to extended and implemented in other chalcogenide systems.

Due to the unique capability of infrared (IR) nonlinear optical (NLO) materials to convert frequencies and produce different wavelengths based on intrinsic light, they are utilized as an essential component in solid-state laser devices within military and civilian fields [1–5]. So far, commercial IR-NLO crystals have been limited in their applications due to inherent defects that lead to low utilization efficiency. For instance, $AgGaS_2$ [6] has a low laser-induced damage threshold (LIDT), $AgGaSe_2$ [7] cannot achieve phase matching (PM) behavior and also has a small LIDT, and $ZnGeP_2$ [8] exhibits severe two-photon absorption. The aforementioned limitations are primarily caused by the narrow band gaps (E_g) of these materials. In addition, there is an incompatible relationship between a wide E_g and a big second–harmonic-generation (SHG) coefficient (d_{eff}) [9–14]. Therefore, it is of great significance and importance to explore new materials that exhibit a well-balanced performance in terms of IR-NLO properties.

In recent decades, extensive research has been conducted on transition metal-based chalcogenides, establishing them as leading candidates for IR-NLO applications [15–19]. Among these chalcogenides, Hg-based ones have gained significant popularity compared to their counterparts, such as Zn and Cd [20]. This popularity is attributed to their unique structural advantages, which include diverse coordination methods like linear $[HgQ_2]$, trigonal-planar $[HgQ_3]$, and tetrahedral $[HgQ_4]$. The highly polarized Hg-Q bonds present in these materials are beneficial for achieving strong effective d_{eff} and significant refractive index variations (Δn). Moreover, Hg-based chalcogenides offer a wider range of IR transmission, covering two crucial atmospheric windows at 3–5 μm and 8–12 μm. So far, all reported Hg-based IR-NLO materials have focused on multivariate systems, such as the chalcogenide

* Corresponding authors.
E-mail addresses: linhua@fjirsm.ac.cn (H. Lin), qlzhu@fjirsm.ac.cn (Q.-L. Zhu).
[1] These authors contributed equally to this work.

https://doi.org/10.1016/j.cclet.2023.109377
1001-8417/

system of $AHgPS_4$ [21] and $AEHgM^{IV}Q_4$ [22–25] (A = alkali-metal elements; AE = alkaline-earth-metal elements; M^{IV} = group 14 elements; Q = chalcogen), as well as the salt-inclusion chalcogenide system of $[Ba_4Cl_2][HgGa_4S_{10}]$ [26] and $[AX][Hg_3P_2S_8]$ (X = halogen) [27]. However, research on ternary systems is relatively scarce. Recently, the ternary transition-metal-rich $M^{II}_4M^{IV}Q_6$ family system has caught our attention, particularly compound Hg_4GeS_6 [28,29]. Despite being reported as early as 1968, it has not yet undergone thorough investigation regarding its NLO performance [30]. Although theoretical calculations indicate a significant d_{eff} of approximately 50 pm/V, preliminary experimental characterization suggests that the SHG signal at of this material is relatively weak under 2050 nm frequency doubling light conditions. This weakness can primarily be attributed to the strong absorption of the both fundamental and frequency-doubled light, which is caused by the material's low optical E_g (*ca.* 1.3 eV). On the other hand, Hg_4GeS_6 possesses a dense 3D tetrahedral-stacking framework. However, due to the slight anisotropy of this structure, its birefringence index is exceedingly small (Δn <0.01), rendering PM unattainable within the working band. Consequently, this limitation hinders its potential for further applications.

In this work, we have implemented a bandgap engineering strategy that involves alkali metal introduction and Hg/Ge ratio regulation to address the limitations of Hg_4GeS_6 mentioned above. The rationale behind this approach is based on the following considerations. Firstly, the introduction of alkali metals with high electronegativity is helpful in obtaining higher E_g. Additionally, it helps in disrupting the original compact structure, leading to the formation of a lower-dimensional structure. This alteration in structure enhances its anisotropy, which in turn results in higher Δn values. Furthermore, by reducing the Hg/Ge ratio, *i.e.*, increasing the Ge content in the component, which can also achieve higher E_g. After multiple attempts, we have successfully obtained two new non-centrosymmetric (NCS) quaternary Hg-based chalcogenides, namely $Rb_2HgGe_3S_8$ and $Cs_2HgGe_3S_8$, using the high-temperature solid-phase method. As anticipated, both compounds exhibit excellent IR-NLO performances including sufficient d_{eff} (0.55–0.70 × $AgGaS_2$), wide E_g (3.27 and 3.41 eV), huge LIDTs (17.4–19.7 × $AgGaS_2$), broad optical transmission intervals (0.32–17.5 μm), and suitable Δn (0.069–0.086@2050 nm). These findings indicate that these compounds hold great potential as candidates for IR-NLO applications. In this report, we will provide details on their synthesis, crystal structures, optical properties, and theoretical calculation analysis.

The crystal structure of Hg_4GeS_6 is significantly complicated, consisting of 4 independent $[HgS_4]$ tetrahedra and 1 $[GeS_4]$ tetrahedra. The three-dimensional (3D) framework can be described as a combination of 3D Hg–Ge–S stacks and 2D Hg–S parts (Fig. 1a, and a more detailed structure is shown in Fig. S1 in Supporting information). In the 3D Hg–Ge–S parts, the $[Hg_2GeS_7]$ layers are connected to each other by sharing S atoms, stacking in an *ABABAB* manner. Within each $[Hg_2GeS_7]$ layer, interesting 12-membered rings (12-MRs) $[Hg_2GeS_9]$ and 6-membered rings (6-MRs) $[Hg_2GeS_7]$ are formed through vertex-sharing $[Hg2S_4]$, $[Hg4S_4]$, and $[GeS_4]$. Each 12-MR is linked to four neighboring 12-MRs and four 6-MRs through Hg/Ge–S bonds. The 2D Hg–S parts are formed by stacking $[Hg_2S_5]$ layers along the a-axis. Within these layers, zigzag 12-MRs $[HgS_3]$ are formed through vertex-sharing $[Hg1S_4]$ and $[Hg3S_4]$. Unfortunately, due to the slight anisotropy of this dense 3D tetrahedral-stacking framework, the Δn index of Hg_4GeS_6 is exceedingly small (<0.01). Therefore, achieving perfect PM feature within the working band is not possible. On the other hand, the high Hg/Ge ratio in the Hg_4GeS_6 results in a low optical E_g (*ca.* 1.3 eV). This low E_g presents a challenge in obtaining a high LIDT, thereby restricting its application in the high-energy laser band. In order to address the limitations of the

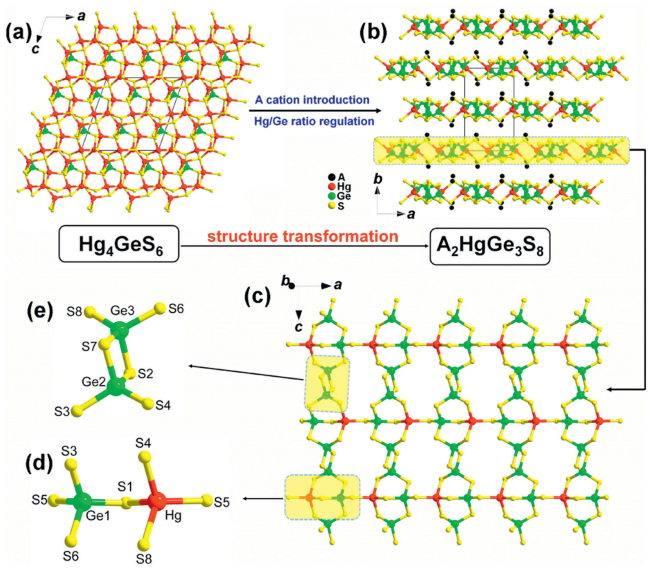

Fig. 1. Structure transformation from (a) 3D Hg_4GeS_6 to (b) 2D $A_2HgGe_3S_8$; (c) A 2D $[HgGe_3S_8]^{2-}$ layer viewed along the *bc* plane with the coordination environment of (d) $[HgGeS_7]$ polyhedron and (e) $[Ge_2S_6]$ dimer marked.

ternary compound Hg_4GeS_6, we have successfully synthesized two quaternary NCS Hg-based chalcogenides, namely $Rb_2HgGe_3S_8$ and $Cs_2HgGe_3S_8$. This achievement was accomplished by employing a bandgap engineering approach, which included the introduction of alkali metals and regulation of the Hg/Ge ratio.

The single X-ray diffraction data accurately correlates to the orthorhombic system [space group: $P2_12_12_1$ (No. 19)]; Pearson symbol: *oP*60; idealized Wyckoff sequence: a^{14}] for $A_2HgGe_3S_8$ (A = Rb, Cs) is accurately correlated. Detailed crystallographic parameters for both compounds are listed in Table S1 (Supporting information). In each unit, there are two crystallographically independent A atoms, one Hg, three Ge, and eight S atoms, all occupying the 4*a* Wyckoff site (Table S2 in Supporting information). As shown in Fig. 1b, $A_2HgGe_3S_8$ (A = Rb, Cs) compounds exhibit a 2D $[HgGe_3S_8]^{2-}$ layer, which is aligned along the *c* axis in the form of *ABABAB* fashion, with A^+ cations inserted to maintain charge balance. Fig. 1c illustrates that each 2D $[HgGe_3S_8]^{2-}$ layer consists of 1D chains composed of $[HgGeS_6]^{6-}$. These 1D chains are linked by $[HgGeS_7]$ tetrahedra (Fig. 1d), alternating *via* corner-sharing along the *a* direction. Moreover, the neighboring chains are linked together into a layer through $[Ge_2S_6]^{4-}$ dimers (Fig. 1e), which share corners along the *c* direction (Fig. 1c). As listed in Tables S3 and S4 (Supporting information), the Hg and Ge atoms are in distorted tetrahedral coordination with 4 S atoms, and the bond lengths of Hg–S and Ge–S are in the ranges of 2.499(3)–2.554(3) Å and 2.156(3)–2.281(3) Å, respectively, which are comparable to those of reported Hg-based and Ge-based chalcogenides [31–38]. In addition, the A^+ cations are coordinated by 8 and 11 S atoms to form $[AS_8]$ and $[AS_{11}]$ polyhedra respectively. The Rb–S bond distances range from 3.373 Å to 4.281 Å, while the Cs–S bond lengths range from 3.467 Å to 4.501 Å (Fig. S2 in Supporting information). These measurements are consistent with the bond distances observed in other alkali-metal sulfides [39–43].

The high-yield bulk crystal $A_2HgGe_3S_8$ (A = Rb, Cs) is synthesized by fully mixing of HgS, Ge, S and RbBr/CsBr at high temperature of 1073 K (experimental details can be found in Supporting information). The experimental powder XRD pattern of $A_2HgGe_3S_8$ (A = Rb, Cs) matches the simulated pattern, indicating that the synthesis process described above can achieve a high phase purity of the crystals (Fig. S3 in Supporting information). SEM and

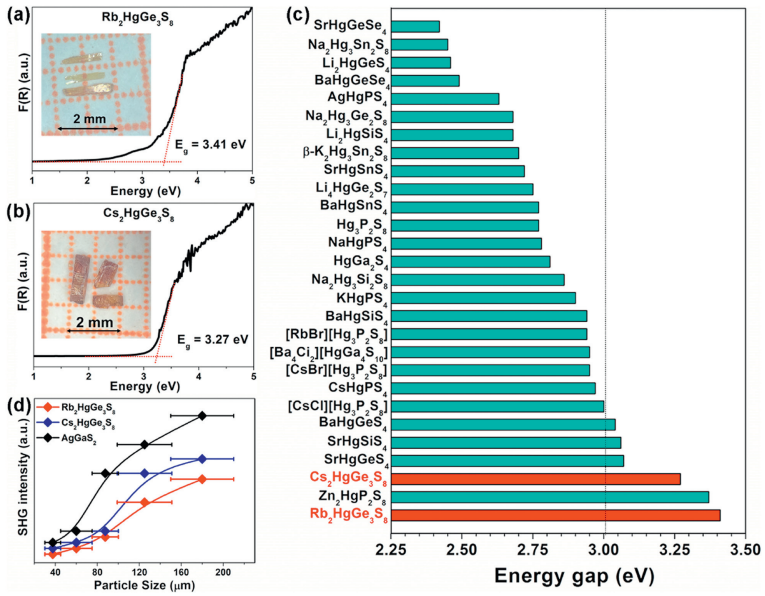

Fig. 2. (a, b) UV–visible–NIR diffuse reflectance spectra of $A_2HgGe_3S_8$ (A = Rb, Cs) based on the powder samples (inset: photographs of the crystals). (c) Comparison of reported IR-NLO Hg-based materials with E_g > 2.33 eV. (d) SHG intensity *vs.* particle size of compounds under 2050 nm laser irradiation.

EDX spectrum analysis were conducted, and the results showed that the compounds had a uniform distribution of A/Hg/Ge/S ratio, with an approximate ratio of 2:1:3:8, which is consistent with the theoretical element content ratio of the title compounds (Fig. S4 in Supporting information). As indicated by UV–vis-NIR absorption spectroscopy, the experimental E_g values are 3.41 and 3.27 eV for $Rb_2HgGe_3S_8$ and $Cs_2HgGe_3S_8$, respectively, which correspond to their crystal colours (the inset in Figs. 2a and b). Comparing the E_g values greater than 2.33 eV (Table S3 in Supporting information) of typical Hg-based IR-NLO chalcogenides in Fig. 2c, only $Zn_2HgP_3S_8$ [44], $AEHgGeS_4$ (AE = Sr, Ba) [25] and $SrHgSiS_4$ [24] have been able to break through the E_g of 3.0 eV. The $A_2HgGe_3S_8$ (A = Rb, Cs) not only surpassed the 3.0 eV E_g, but $Rb_2HgGe_3S_8$ also possesses the largest E_g (3.41 eV) among all reported Hg-based IR-NLO materials. It is worth noting that in the $A_2M^{II}M^{IV}{}_3Q_8$ system (A = alkali-metal elements; M^{II} = divalent transition-metal elements, M^{IV} = group 14 elements, Q = chalcogen) with space groups of $P2_1$, $P2_1/c$ and $P2_12_12_1$, there is a strong correlation between the experimental E_g (measured in eV) and the cell volume (measured in Å^3) of the reported compounds (Fig. S5 in Supporting information). This correlation can be calculated using the formula $E_g = -0.0041 \times V + 9.5448$ (with an R^2 value of 0.878). In addition, the IR spectra (Fig. S6 in Supporting information) indicate that there are no noticeable absorption peaks in the range of 4000–600 cm^{-1}, suggesting that $A_2HgGe_3S_8$ (A = Rb, Cs) possess a wide IR transmission region. Specifically, $Rb_2HgGe_3S_8$ has a transmission region of 17.2 μm, while $Cs_2HgGe_3S_8$ has a transmission region of 17.5 μm. This enables coverage of two important atmospheric windows, which are the 3–5 μm and 8–12 μm ranges. As shown in Fig. S7 (Supporting information), the TG-DSC curves of $A_2HgGe_3S_8$ (A = Rb, Cs) indicate no significant weight loss until reaching 800 K. However, as the temperature increases further, the title compounds undergo decomposition, which can be confirmed by powder XRD results (Fig. S8 in Supporting information).

The powder SHG measurements of $Rb_2HgGe_3S_8$ and $Cs_2HgGe_3S_8$ were carried out under laser irradiation at 2050 nm using the modified Kurtz–Perry method [45]. It was observed that there is a positive correlation between the particle size and SHG intensity, indicating that both compounds exhibit type-I PM behavior (Fig. 2d). In the particle size range of 150–210 μm, the SHG intensities of $Rb_2HgGe_3S_8$ and $Cs_2HgGe_3S_8$ are approximately 0.55 and 0.70 times that of the benchmark $AgGaS_2$, respectively. To the best of our knowledge, both compounds are the first examples of NLO activity among all reported $A_2M^{II}M^{IV}{}_3Q_8$ systems with a space group of $P2_12_12_1$, breaking the trade-off relationship between large E_g (>3.0 eV) and sufficient d_{eff} (>0.5 × $AgGaS_2$) in Hg-based IR-NLO chalcogenides (Table S4 in Supporting information). The E_g is a major factor that affects the LIDT, and a wide E_g is beneficial for achieving high LIDT [46–49]. The measured power LIDTs [50] of $Rb_2HgGe_3S_8$ and $Cs_2HgGe_3S_8$ are 49.1 and 55.4 MW/cm^2, respectively, which is approximately 17.4 times and 19.7 times that of $AgGaS_2$ (2.82 MW/cm^2) [51–55].

To investigate the relationship between NCS structure and optical performance, we conducted a study on the electronic structure of the title compounds using first-principles computational methods [56,57]. The electron band structures reveal that the minimum value of the conduction band (CB) and the maximum value of the valence band (VB) occur at different points, indicating an indirect E_g for the product. The calculated E_g values are 2.16 eV and 2.19 eV, respectively (Fig. S9 in Supporting information) and the first Brillouin zone with high symmetry points was provided in Fig. S10 (Supporting information). However, it is important to note that due to the discontinuity of the exchange-related energy of the GGA functionals, the theoretical calculated E_g value will be lower than the experimentally measured one [58,59]. We also utilized the PBE approach to calculate the partial densities of states (PDOS) of $A_2HgGe_3S_8$ (A = Rb, Cs) in the energy range from −10 eV to 10 eV. These results are displayed in Figs. 3a and b. According to the PDOS, it can be observed that the contribution of VB maximum is minimum S-3p and Hg-5d orbitals, with a small contribution from Hg-6p orbitals. Conversely, the contribution of CB minimum is mainly arises from Ge-4s and S-3p orbitals, with a small contribution from Ge-4p and Hg-6s orbitals. Based on these findings, we can deduce that the optical band gap primarily consists of Ge-4s, S-3p, Hg-5d orbitals. Therefore, the optical band gap of $A_2HgGe_3S_8$ (A = Rb, Cs) is primarily determined by the functional units [GeS_4] and [HgS_4].

Due to the restriction of Kleinman symmetry [60], $A_2HgGe_3S_8$ (A = Rb, Cs) belongs to the orthogonal space group, with only one independent nonzero second-order nonlinear coefficient,

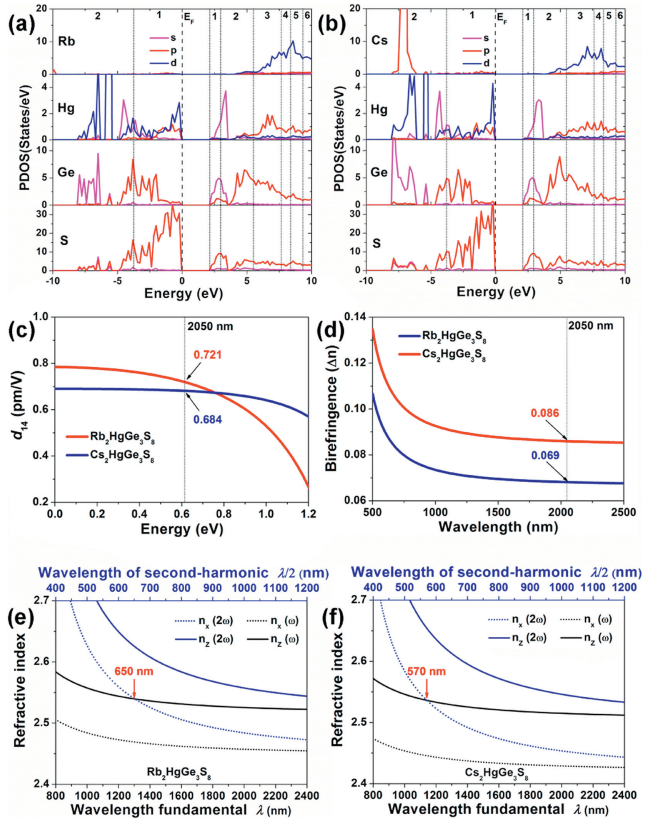

Fig. 3. Theoretical calculation results of $A_2HgGe_3S_8$ (A = Rb, Cs): (a, b) PDOS; (c) frequency-dependent SHG coefficient d_{14}; (d) theoretical birefringence (Δn); (e, f) the calculated shortest type-I PM cut-off wavelength.

i.e., $d_{14} = d_{25} = d_{36}$. The calculated results for $Rb_2HgGe_3S_8$ and $Cs_2HgGe_3S_8$ are 0.721 pm/V and 0.684 pm/V at the wavelength of 2050 nm, respectively (Fig. 3c), which is consistent with the trend obtained from the experiment. Additionally, the theoretically calculated Δn values for $Rb_2HgGe_3S_8$ and $Cs_2HgGe_3S_8$ at 2050 nm are 0.086 and 0.069 (Fig. 3d), respectively. The moderate Δn index is conducive to PM, and the experimental results also confirmed that the title compounds exhibit PM behaviour. According to the condition of type-I phase matching [$n_e(2\omega) = n_o(\omega)$], where n_e and n_o represent the refractive index of extraordinary light and ordinary light, respectively, it can be concluded that the shortest PM cut-off edges for $Rb_2HgGe_3S_8$ and $Cs_2HgGe_3S_8$ are 650 nm and 570 nm, respectively (Figs. 3e and f) [61–64].

In order to further investigate the source of the SHG effect, we conducted a detailed analysis of the cut-off energy dependent static d_{14} based on the length specification [65,66], as shown in Fig. 4. The results indicate that d_{14} exhibits an upward trend in the VB-1 (−3.8∼0.0 eV), CB-1 (2.1–3.0 eV), CB-3 (5.5–7.7 eV), and CB-5 (8.4–9.3 eV) regions. This implies that these four regions play a crucial role in the SHG response. By considering the charge density of PDOS and related components, we can conclude that the SHG response is a result of the synergistic effect between the NLO-activity [HgS_4] and [GeS_4] BBUs, specifically within the 2D $[HgGe_3S_8]^{2-}$ layer.

In conclusion, the introduction of alkali metals and regulation of the Hg/Ge ratio in the ternary narrow-band-gap parent Hg_4GeS_6 has led to the successful discovery and systematic characterization of two new Hg-based IR-NLO chalcogenides, namely $Rb_2HgGe_3S_8$ and $Cs_2HgGe_3S_8$. These compounds belong to the NCS $P2_12_12_1$ space group and exhibit interesting 2D layered structures composed of [HgS_4] and [GeS_4] tetrahedra. They demonstrate excellent performance balance in terms of PM d_{eff} (0.55–0.70 × $AaGgS_2$), E_g (3.27–3.41 eV), optical transparency window (0.32–17.5 μm), and LIDTs (17.4–19.7 × $AaGgS_2$). Furthermore, detailed theoretical studies support the notion that tetrahedral [HgS_4] and [GeS_4] motifs play a pivotal role in the enhancing d_{eff} and E_g of these materials. This research expands our understanding of the structure-activity relationship of Hg-based chalcogenides and contributes to the design of high-performance IR-NLO candidates.

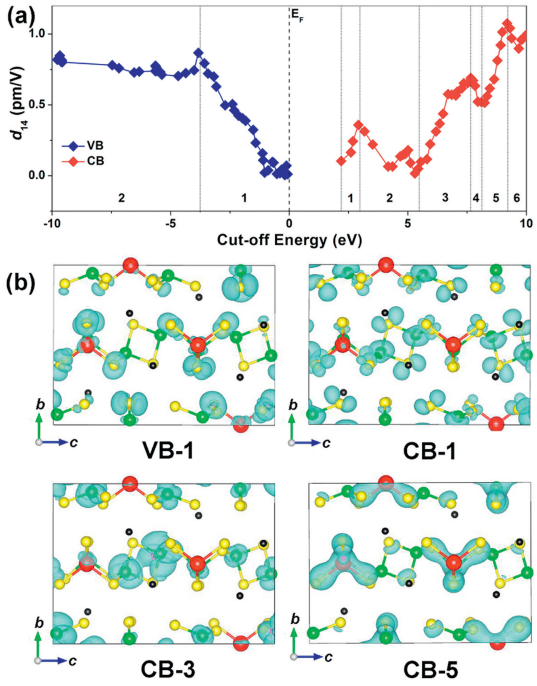

Fig. 4. Theoretical analysis of the SHG source: (a) Cut-off-energy-dependent variation of static coefficient d_{14}; (b) charge density maps in the VB-1, CB-1, CB-3, and CB-5 regions along the *bc* plane.

Declaration of competing interest

The authors declare that they have no known competing financial interests or personal relationships that could have appeared to influence the work reported in this paper.

Acknowledgments

This work was supported by the National Natural Science Foundation of China (Nos. 22175175 and 22193043), Natural Science Foundation of Fujian Province (Nos. 2022L3092 and 2023H0041), Fujian Science & Technology Innovation Laboratory for Optoelectronic Information of China (No. 2021ZR118), and the Youth Innovation Promotion Association CAS (No. 2022303). The authors thank Prof. Bing-Xuan Li at FJIRSM for helping with the NLO measurements and Prof. Yong-Fan Zhang at Fuzhou University for helping with the DFT calculations.

Supplementary materials

Supplementary material associated with this article can be found, in the online version, at doi:10.1016/j.cclet.2023.109377.

References

[1] F.J. Duarte, Chapters 2, 9 and 12, Tunable Laser Applications, CRC Press, Boca Raton, FL, 2008.
[2] V. Petrov, Prog. Quantum Electron. 44 (2015) 1–106.

[3] V.A. Serebryakov, E.V. Boiko, N.N. Petrishchev, et al., J. Opt.Technol. 77 (2010) 6–17.
[4] X.T. Wu, L. Chen, Struct. Bonding 145 (2012) 1–42.
[5] N.L.B. Sayson, T. Bi, V. Ng, et al., Nat. Photonics 13 (2019) 701–706.
[6] G.D. Boyd, E. Buehler, F.G. Storz, Appl. Phys. Lett. 18 (1971) 301–304.
[7] G.C. Catella, L.R. Shiozawa, J.R. Hietanen, et al., Appl. Opt. 32 (1993) 3948–3951.
[8] A. Harasaki, K.J. Kato, Appl. Phys. 36 (1997) 700–703.
[9] L. Kang, M.L. Zhou, J.Y. Yao, et al., J. Am. Chem. Soc. 137 (2015) 13049–13059.
[10] S.P. Guo, Y. Chi, G.C. Guo, Coord. Chem. Rev. 335 (2017) 44–57.
[11] K. Wu, S.L. Pan, Coord. Chem. Rev. 377 (2018) 191–208.
[12] H. Lin, W.B. Wei, H. Chen, et al., Coord. Chem. Rev. 406 (2020) 213150.
[13] W.K. Wang, D.J. Mei, F. Liang, et al., Coord. Chem. Rev. 421 (2020) 213444.
[14] M.Y. Ran, A.Y. Wang, W.B. Wei, et al., Coord. Chem. Rev. 481 (2023) 215059.
[15] H. Chen, W.B. Wei, H. Lin, et al., Coord. Chem. Rev. 448 (2021) 214154.
[16] H. Chen, M.Y. Ran, W.B. Wei, et al., Coord. Chem. Rev. 470 (2022) 214706.
[17] W. Zhou, J. Wu, W. Liu, et al., Coord. Chem. Rev. 477 (2023) 214950.
[18] F. Hou, D.M, Y. Zhang, et al., J. Alloys Compd. 904 (2022) 163944.
[19] M. Ma, J. Dang, Y. Wu, et al., Inorg. Chem. 62 (2023) 6549–6553.
[20] C.X. Li, X.H. Meng, Z. Li, et al., Coord. Chem. Rev. 453 (2022) 214328.
[21] W. Xing, C. Tang, P. Gong, et al., Inorg. Chem. 60 (2021) 18370–18378.
[22] Y. Guo, F. Liang, Z. Li, et al., Inorg. Chem. 58 (2019) 10390–10398.
[23] Y. Guo, F. Liang, W. Yin, et al., Chem. Mater. 31 (2019) 3034–3040.
[24] X.Y. Zhang, H.P. Wu, Z.G. Hu, et al., Adv. Optical Mater. 11 (2023) 2301735.
[25] M.Y. Ran, S.H. Zhou, W.B. Wei, et al., Small 20 (2024) 2304563.
[26] Y. Zhang, H. Wu, Z. Hu, et al., Inorg. Chem. Front. 9 (2022) 4075–4080.
[27] W. Xing, C. Tang, N. Wang, B. Kang, et al., Adv. Opt. Mater. 9 (2021) 2100563.
[28] M.Y. Li, B.X. Li, H. Lin, et al., Inorg. Chem. 57 (2018) 8730–8734.
[29] J.D. Chen, C.S. Lin, S.D. Yang, et al., Cryst. Growth Des. 20 (2020) 2489–2496.
[30] J. Serment, G. Perez, P. Hagenmuller, Bull. Soc. Chim. Fr. 2 (1968) 561–566.
[31] K. Wu, Z. Yang, S. Pan, Chem. Mater. 28 (2016) 2795–2801.
[32] K. Wu, Z. Yang, S. Pan, Chem. Commun. 53 (2017) 3010–3013.
[33] W. Xing, C. Tang, N. Wang, et al., Inorg. Chem. 59 (2020) 18452–18460.
[34] Z. Yang, Y. Yang, Y. Guo, et al., Chem. Mater. 31 (2019) 1110–1117.
[35] M.Y. Li, Z.J. Ma, B.X. Li, et al., Chem. Mater. 32 (2020) 4331–4339.
[36] M. Yan, Z.D. Sun, W.D. Yao, et al., Inorg. Chem. Front. 7 (2020) 2451–2458.
[37] D. Mei, W. Cao, N. Wang, et al., Mater. Horiz. 8 (2021) 2330.
[38] W. Wang, D. Mei, S. Wen, et al., Chin. Chem. Lett. 33 (2022) 2301–2315.
[39] H. Lin, L.J. Zhou, L. Chen, Chem. Mater. 24 (2012) 3406–3414.
[40] H. Lin, H. Chen, Y.J. Zheng, et al., Chem. Eur. J. 23 (2017) 10407–10412.
[41] M.M. Chen, S.H. Zhou, W.B. Wei, et al., Adv. Optical Mater. 10 (2022) 2102123.
[42] M.M. Chen, S.H. Zhou, W.B. Wei, et al., ACS Mater. Lett. 4 (2022) 1264–1269.
[43] H. Chen, M.Y. Ran, S.H. Zhou, et al., Chin. Chem. Lett. 34 (2023) 107838.
[44] Y. Chu, H.S. Wang, T.D. Abutukadi, et al., Small 20 (2024) 2305074.
[45] S.K. Kurtz, T.T. Perry, J. Appl. Phys. 39 (1968) 3798–3813.
[46] M.Y. Ran, S.H. Zhou, W.B. Wei, et al., Small 19 (2023) 2300248.
[47] H.D. Yang, M.Y. Ran, W.B. Wei, et al., Mater. Today Phys. 35 (2023) 101127.
[48] M.Y. Ran, Z. Ma, H. Chen, et al., Chem. Mater. 32 (2020) 5890–5896.
[49] J.X. Zhang, M.Y. Ran, X.T. Wu, et al., Inorg. Chem. Front. 10 (2023) 5244–5257.
[50] M.J. Zhang, X.M. Jiang, L.J. Zhou, et al., J. Mater. Chem. C 1 (2013) 4754–4760.
[51] M.Y. Li, B.X. Li, H. Lin, et al., Chem. Mater. 31 (2019) 6268–6275.
[52] H. Chen, Y.Y. Li, B.X. Li, et al., Chem. Mater. 32 (2020) 8012–8019.
[53] H.D. Yang, M.Y. Ran, S.H. Zhou, et al., Chem. Sci. 13 (2022) 10725–10733.
[54] Y.F. Shi, Z. Ma, B.X. Li, et al., Mater. Chem. Front. 6 (2022) 3054–3061.
[55] M.Y. Ran, S.H. Zhou, B.X. Li, et al., Chem. Mater. 34 (2022) 3853–3861.
[56] S.N. Rashkeev, W.R.L. Lambrecht, B. Segall, Phys. Rev. B 57 (1998) 3905–3919.
[57] Z. Fang, J. Lin, R. Liu, et al., CrystEngComm 16 (2014) 10569–10580.
[58] K.J. Burke, Chem. Phys. 136 (2012) 150901.
[59] K. Govaerts, R. Saniz, B. Partoens, et al., Phys. Rev. B: Condens. Matter Mater. Phys. 87 (2013) 235210.
[60] D.A. Kleinman, Phys. Rev. 126 (1962) 1977.
[61] M.M. Chen, Z. Ma, B.X. Li, et al., J. Mater. Chem. C 9 (2021) 1156.
[62] Y. Xiao, M.M. Chen, Y.Y. Shen, et al., Inorg. Chem. Front. 8 (2021) 2835.
[63] C. Liu, S.H. Zhou, Y. Xiao, et al., J. Mater. Chem. C 9 (2021) 15407.
[64] H. Lin, Y.Y. Li, M.Y. Li, et al., J. Mater. Chem. C 7 (2019) 4638–4643.
[65] C. Aversa, J.E. Sipe, Phys. Rev. B 52 (1995) 14636.
[66] S.N. Rashkeev, W.R.L. Lambrecht, B. Segall, Phys. Rev. B. 57 (1998) 3905.